Bull. Chem. Soc. Jpn., 72, 2655—2664 (1999)

^{89}Y MAS NMR in Red Phosphor, Eu-Doped Y_2O_2S. Assignment of Peaks Shifted by Paramagnetic Eu^{3+}, Spin Lattice Relaxation Time, and Eu Distribution

Toshie Harazono,* Ryuji Adachi,† Naoto Kijima, and Tokuko Watanabe††

Research Center, Mitsubishi Chemical Co., Ltd., 1000, Kamoshida, Aoba-ku, Yokohama 227-8502

†Phosphor R & D Department, Kasei Optonix Co., Ltd., 1060, Naruta, Odawara, Kanagawa 250-0862

††Tokyo University of Fisheries, 4-5-7, Konan, Minato-ku, Tokyo 108-8477

(Received June 22, 1999)

^{89}Y MAS (Magic angle spinning) NMR has been investigated to study the local environment of Y sites in a red phosphor, Eu doped-Y_2O_2S (Eu–Y_2O_2S), with varying the Eu content. Despite the presence of paramagnetic Eu^{3+} ions, high resolution spectra were acquired and a number of local environments were detected. The assignment of the resonances to different Y local environments was made on the basis of signal intensities, chemical shifts, and spin-lattice relaxation times (T_1) in conjugation with the crystal structural data which were obtained by the Rietveld method. Besides the main peak in pure Y_2O_2S, four peaks caused by the $\underline{Y^1}$–Eu species and ten peaks caused by the Eu–$\underline{Y^1}$–Eu species were distinguished in Eu–Y_2O_2S, where Y^1 is the next nearest-neighbor Y site for the doped Eu atom, and $\underline{Y^1}$–Eu and Eu–$\underline{Y^1}$–Eu are substituted by one and two Eu, respectively. Y atoms (Y^2, Y^3, $\cdots$ Y^n), which are further from the second and more nearest-neighbors from Eu were observed at the same resonance position for all samples investigated with that of pure Y_2O_2S.

The T_1 values of the ^{89}Y signal were reduced from 6.6 h for pure Y_2O_2S to 230 s (10 mol% Eu–Y_2O_2S) for Y^n ($n \geq 2$), to several tens of seconds for Y^1–Eu and to several seconds for Eu–Y^1–Eu in Eu–Y_2O_2S. The Eu content to Y in the region where Eu atoms are randomly isolated was estimated from the intensity ratio of the total intensities of the four Y^1 peaks to the main peak. T_1 reduction and a line-broadening due to paramagnetic Eu^{3+} ions are discussed in relation to the distribution of Eu ions.

The incorporation of paramagnetic ions into a local coordination sphere surrounding a resonating nucleus in solid materials causes a paramagnetic shift, line-broadening, an overlapping of the signals and an enhanced side band intensity in MAS NMR spectra. On the other hand, it allows many different local environments to be detected.[1—10] MAS NMR can remove a large anisotropic broadening (i.e., dipolar and chemical shift anisotropies) and ascertain the influence of the local coordination and the next nearest-neighbor paramagnetic ion on the isotropic chemical shift.

Recently, assignments of the resonances to different lithium local environments were made by comparing the observed shifts in the ^6Li MAS NMR spectra and local structures in a number of lithium manganates.[7] The shifts are ascribed primarily to a Fermi-contact shift mechanism.

It was shown that the isotropic chemical shift for the ^{89}Y nucleus is dependent on the number and type of atoms of the next and the second nearest-neighbors, which are not only paramagnetic, but also diamagnetic atoms.[4,11—17]

In a series of rare-earth stannates, $Ln_2Sn_2O_7$ and titanates $Ln_2Ti_2O_7$, a very large variation of the ^{119}Sn chemical shifts (from approximately +5400 to −4200 ppm) was caused by lantanide ions, except for Gd, which were attributed principally to the Fermi-contact shift mechanism.[3] Furthermore, five new peaks result from changes in the local coordination when Sm^{3+} substitutes for Y^{3+} in the $Y_2Sn_2O_7$.[3] The shifts due to the local environment in ^{89}Y MAS NMR signals was explained by a through-space dipolar mechanism (pseudocontact interaction).[4]

The authors applied ^{89}Y static and MAS NMR to the phosphors, Eu–Y_2O_3 and Tb–$Y_3Al_5O_{12}$.[16,17] In Tb–$Y_3Al_5O_{12}$ with increasing content of doped Tb, extra peaks appeared near to the main peak at 239 ppm in the ^{89}Y MAS NMR spectra, and their chemical shifts were discussed based on the pseudocontact mechanism. The extra peaks were assigned to the second to the fifth nearest-neighbor Y (Y^2, Y^3, Y^4, and Y^5) atoms to the Tb atom via the intervening coordinated oxygen atoms.[17] A red phosphor, Eu–Y_2O_3, and a green phosphor, Tb–$Y_3Al_5O_{12}$, have been used in color picture tubes. The brightness of these phosphors is strongly related to the local environment of the Y centers in lanthanide-doped phosphors. In these investigations it was found that ^{89}Y MAS NMR plays a useful role in probing the properties of phosphors, and that the randomness of the distribution of paramagnetic ions in the mother crystallites is the most important factor concerning the high brightness of the phosphors.[16,17] In this paper, we present the results from the ^{89}Y MAS NMR study of a series of Eu–Y_2O_2S red phosphors with 0 to 10 mol% content of Eu/Y. By incorporating Eu, fourteen new peaks appeared. The aim of this study was

to determine the fourteen local coordination environments of Y atoms surrounded by paramagnetic Eu^{3+} ions with the $4f^6$ electron configuration and to characterize the distribution of Eu atoms in the mother crystallites. For this purpose, precise crystal structures of Y_2O_2S and Eu–Y_2O_2S were determined by the Rietveld method first, and then spin-lattice relaxation times (T_1) of each species and chemical shifts were considered. The chemical shift deviation of the 14 newly appearing peaks from the main peak for Y_2O_2S was explained by paramagnetic (contact and pseudocontact) shifts. The contribution of the contact and pseudocontact shifts to the paramagnetic shift of the peak was not quantitatively interpreted from the data in this investigation.

Experimental

Materials: All of the samples used in this study are listed in Table 1. The raw materials, Y_2O_3 and Eu_2O_3, were prepared by Mitsubishi Kasei Co., Ltd., and the other materials were purchased from Wako Co., Ltd., Junsei Co., Ltd., and Kanto Chemical Co., Ltd. The raw material Y_2O_3 contained Tb_4O_7 at about 28 ppm as a photosensitive material. The other raw material, Eu_2O_3, was of luminescence grade, and all other materials were of reagent grade.

The samples employed in this investigation were prepared by the method described in the handbook of phosphors[18] and patents.[19,20] The preparation procedures were as follows: Na_2CO_3, K_3PO_4, and S were added to raw materials, Y_2O_3 and Eu_2O_3, as the flux in an alumina crucible; the mixture was fired at 1200 °C for several hours. Eu–Y_2O_2S samples prepared by the above methods were washed with pure water several times and dried. Each molar ratio, Eu/Y, and the amounts of impurity were determined by GD-MS VD9000, Seiko-SPS-1200A ICP, and Rigaku 3370 X-ray fluorescence spectrometers. The amounts of impurities in all samples except Y_2O_3 with 28 ppm content of Tb_4O_7 were less than 1 ppm. The Tb content in Eu–Y_2O_2S samples prepared were analyzed as 10 ppm. The activator content was consistent with the analytical concentration of Eu within the experimental error. The chemical compositions of the samples used for crystal structure refinement by the Rietveld analysis were pure Y_2O_2S (KR1) and $(Y_{0.9091},Eu_{0.0909})_2O_2S$ (KR6).

Apparatus and Measurements: X-Ray powder diffraction data of Y_2O_2S and the Eu-doped Y_2O_2S were collected at room temperature by a Rigaku RINT-1500 X-ray diffractometer equipped with a curved graphite monochromator in the scattering beam path. The diffraction intensities were measured by step-scannings in the ranges of 10° to 120° in 2θ with the step width of 0.04° and the measuring time of 4 seconds using Cu $K\alpha$ radiation.

An analysis by the Rietveld method was carried out by means of the RIETAN program.[21] The space group of Y_2O_2S was $P\bar{3}m1$ (No. 164), which is identical with that of La_2O_2S. Supposing that Y_2O_2S has a similar crystal structure to that of La_2O_2S, we referred the atomic parameters of La_2O_2S as the initial values for the analysis. The crystal structure of the Eu-doped Y_2O_2S was analyzed under the assumption that Eu atoms partially occupy the Y site.

The emission spectra and the brightness excited by an electron beam were measured with a TOPCON ABT-32 spectrometer. Furthermore, the emission spectra excited by the light with a wavelength of 254 nm and the intensities of 624 nm peaks ($^5D_0 \rightarrow {}^7F_2$)[22] were measured by a Fluorescence Spectrophotometer, F-4500 (Hitachi). The emission pattern of Eu–Y_2O_2S showed the maximum intensity peak at 624 nm.[23] The brightness (%) of Eu–Y_2O_2S excited by the electron beam, as well as the peak intensity at 624 nm in the luminescence spectra excited by the light with the wavelength of 254 nm, is tabulated in Table 1. The particle size was measured with a Model PA-2 Coulter Counter.

^{89}Y MAS and static NMR measurements were carried out at 14.706 MHz on a Bruker MSL-300 spectrometer (7.05 T) equipped with a low frequency CP (cross polarization) MAS probe (dia. 7 mm) at a spinning rate of 5 kHz and a static probe (dia. 10 mm), respectively. 90° pulse widths were 11 μs (MAS) and 15 μs (static). Chemical shifts were determined relative to a 1.5 M $Y(NO_3)_3$ aqueous solution (1 M = 1 mol dm^{-3}) as 0 ppm for ^{89}Y. A single pulse was used for MAS and static measurements. All measurements were performed at room temperature.

Results

^{89}Y Static and MAS NMR Spectra: The ^{89}Y static and MAS spectra of Eu–Y_2O_2S (KR2 to KR6) are given in Figs. 1a and 1b, respectively, together with those of pure Y_2O_2S (KR1) for a comparison. The ^{89}Y static NMR spectra show the maximum intensity at the nearly 234 ppm (corresponding to $\sigma_\perp$).[15] For all Eu–Y_2O_2S samples, four additional peaks appear besides of the central peak at 292 ppm and the significant line-broadening of the signals occur with increasing in Eu content. These five peaks, including the central peak, are labeled symbolically ①, ②, ③, ④, and ⑤, respectively, in order from the high frequency side as shown in Fig. 1b. The linewidth at half-height for peak ③ (in KR1 to KR6) was proportional to the Eu content, which is shown in Fig. 2.

The ^{89}Y MAS spectra of a sample with 10 mol% Eu (KR6) detected at the short recycle times of 2, 50, and 249 s are demonstrated in Fig. 3. As results, 10 other peaks labeled (a), (b), (c), --- (j) newly appear besides peaks ① to ⑤.

Spin-Lattice Relaxation Times (T_1) of ^{89}Y Resonance: The saturation recovery curve of the main peak (292 ppm, ③) in pure Y_2O_2S was fitted by a single T_1 (6.61 h).[15] On the

Table 1. Sample List of Eu–Y_2O_2S

Sample	Eu/Y	$(Y_{1-c}Eu_c)_2O_3$		Chroma	Particle size	Brightness[b]	Intensity of 624 nm peak[c]
	mol%	$1-c$	c[a]	x/y[32]	$d_{50}/\mu m$	%(arbitrary)	%(arbitrary)
KR1	0	1.00	0.00	230/244	6.8	44	—
KR2	1	0.9901	0.0099	554/403	6.3	197	80.6
KR3	2	0.9804	0.0196	604/375	6.8	164	92.7
KR4	4	0.9614	0.0384	649/342	6.1	123	100
KR5	7	0.9346	0.0654	669/326	6.4	84	95.5
KR6	10	0.9091	0.0909	673/322	5.8	57	93.2

a) Incorporated activator content. b) Excited by the electron beam. c) Excited by the light with the wavelength of 254 nm.

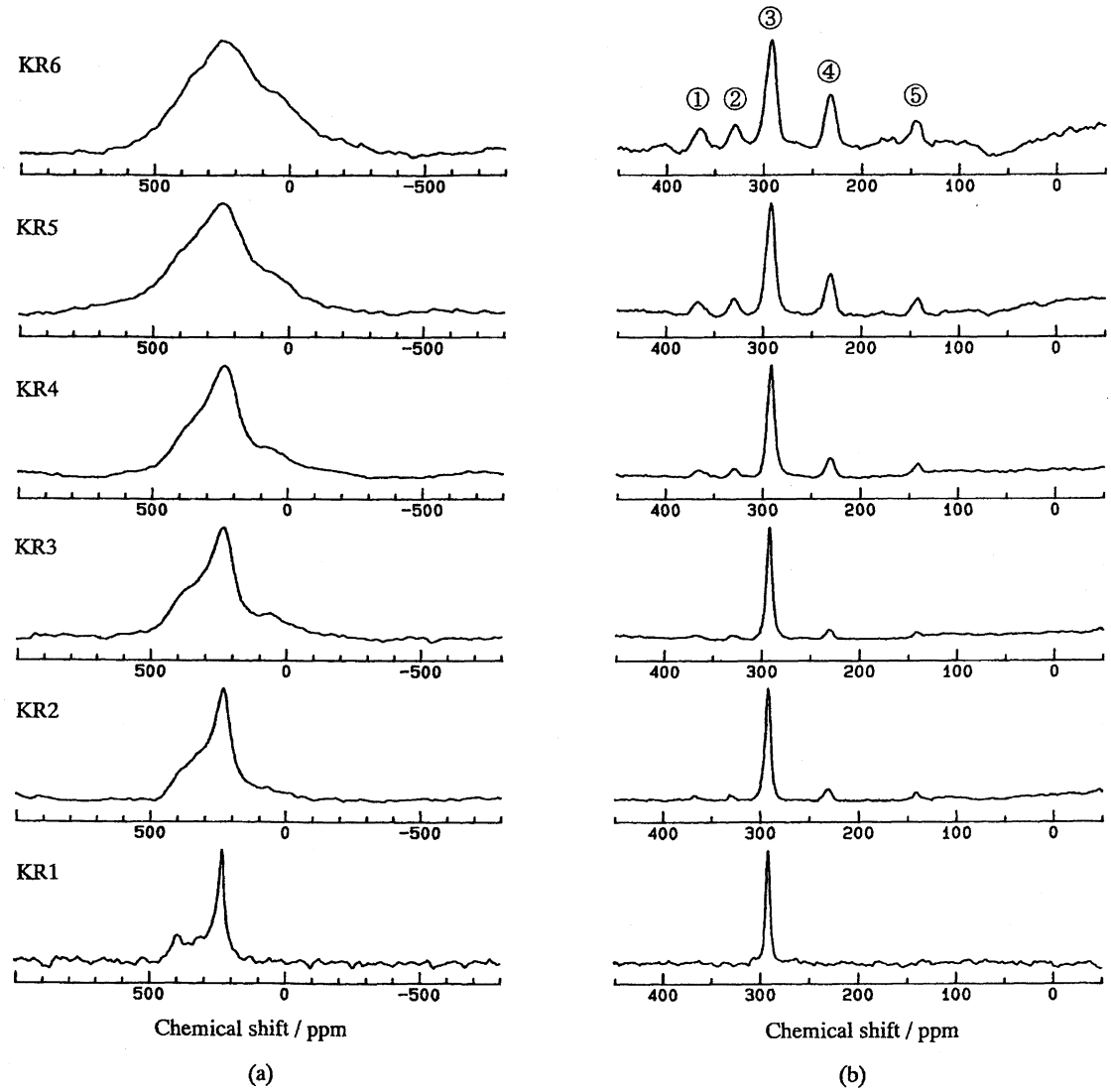

Fig. 1. ^{89}Y solid state NMR spectra of Eu–Y_2O_2S. (a): Static NMR spectra of KR1 to KR6. Spectral width: 200000 Hz, data point: 8K, 90° pulse: 15 μs, pulse width: 5 μs, aquisition number: 3300—17000, recycle time: KR1; 1000 s, KR2–KR6; 10 s, dead time: 50μs. (b): MAS NMR spectra of KR1 to KR6. Spectral width: 15000 Hz, data point: 4 K, 90° pulse: 11μs, aquisition number: 1 to 250 times, recycle time: KR1; 150000 s, KR2; 1000 s, KR3; 7500 s, KR4; 5000 s, KR5; 1600 s, KR6; 1200 s, spinning rate: 5000 rps, dead time: 150 μs.

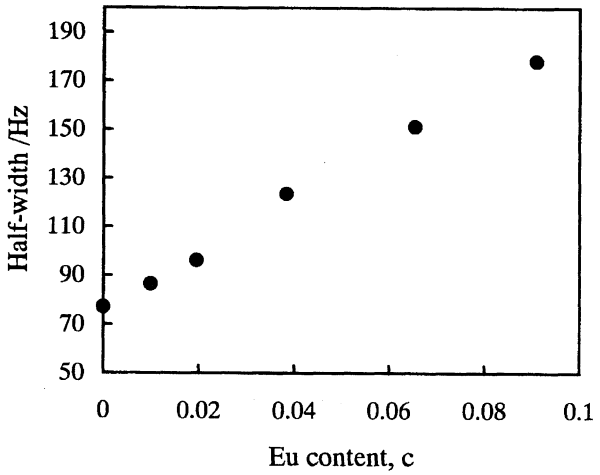

Fig. 2. Relationship between the peak width at half-height and the Eu content.

other hand, the saturation recovery curves of the main peaks for Eu–Y_2O_2S (KR2 to KR6) showed at least two different T_1, T_{1S}, and T_{1L}. The shorter T_{1S} was approximately several seconds (5 to 19 s) and no clear relation to the Eu content was found. The population of the shorter component was about 10% for all samples. As listed in Table 2, the longer T_{1L} showed the Eu content dependence. T_{1L} of peak ③ reduced from 23800 s (6.61 h) for pure Y_2O_2S to 230 s (3.83 min) for KR6, as a function of Eu content. The saturation recovery curves of the additional peaks ①, ②, ④, and ⑤ for KR2 to KR6 closely fit by one T_1, and the T_1 ranging from 18 to 148 s was also independent of the Eu content as tabulated in Table 2. The T_1 for peaks (b), (e), (g), and (i) in Fig. 3 were very short and in the range of 11 s to 43 s, as shown in Table 7 (right most column).

The MAS spectra for KR3 to KR6 demonstrated in Fig. 1b were obtained by accumulating after a recycle time of about

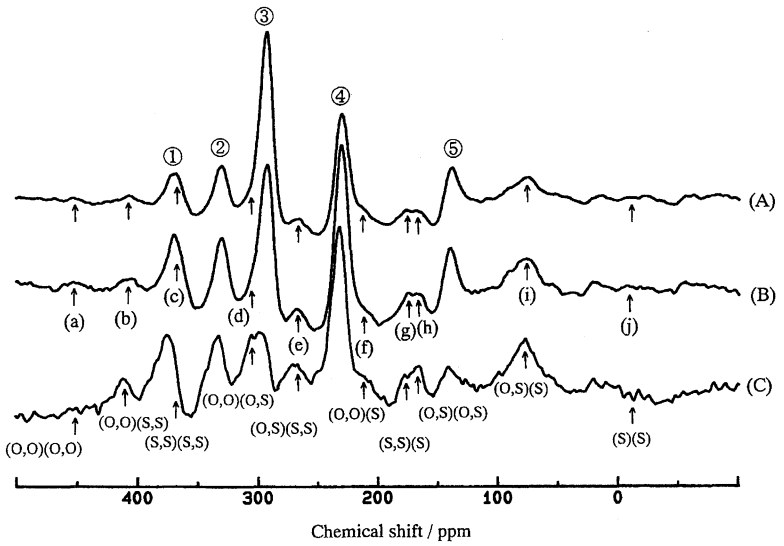

Fig. 3. The ^{89}Y MAS spectrum of KR6 with 10 mol% content of Eu. Spectral width: 15000 Hz, data point: 2 or 4 K, 90° pulse: 11 μs, aquisition number: 1152—4150 times, spinning rate: 5000 rps, dead time: 150 μs, recycle time: (A); 249 s, (B); 50 s, (C); 2 s.

Table 2. Spin-Lattice Relaxation Times, Observed and Calculated Y^1/Y^n, and the Eu Concentration in the Randomly Distributed Area of Eu–Y_2O_2S

sample	T_1/s					Y^1/Y^n		Eu concn	Recycle time
	①[b]	②[b]	③[a]	④[b]	⑤[b]	obsd	calcd	calcd	s
KR1	/	/	23800	/	/	/	/		150000
KR2	20	34	2460	36	145	/	0.176/1		1000
KR3	17	39	1560	36	157	0.25/1	0.428/1	0.013	7500
KR4	17	30	890	31	143	0.53/1	1.494/1	0.023	5000
KR5	21	42	370	33	164	0.93/1	/	0.031	1600
KR6	16	46	230	36	133	1.31/1	/	0.036	1200
Ave.	18.2	38.2	/	34.4	148.4	/	/		/

T_1 of five peaks were measured by the saturation recovery method. a) The peak intensities of ③ for KR2 to KR6 were fitted by employing the non-linear least square method with two components, long (L) and short (S) components. The shorter components T_{1S} (about 10%) were about several seconds. The longer T_{1L} is presented for KR2 to KR6. The peak ③ for KR1 was fitted by a single T_1. b) The saturation recovery curves were fitted by one T_1.

5 times the longer T_{1L} of peak ③. The relative values of the area of the peaks ①, ②, ④, and ⑤ were almost precisely 1 : 1 : 2 : 1. The ratio of the total peak area for ①+②+④+⑤ to that for peak ③ is shown as Y^1/Y^n ($n \geq 2$) in Table 2.

Crystal Structure of Pure Y_2O_2S and Eu–Y_2O_2S: Table 3 shows the refined atomic parameters of the crystal structure of pure Y_2O_2S (KR1). The atomic parameters of the Eu–Y_2O_2S (KR6) were the same as those of pure Y_2O_2S within the experimental errors. The lattice parameters were refined to a = 3.784(2) and c = 6.587(4) Å for Y_2O_2S and a = 3.792(2) and c = 6.596(4) Å for the Eu–Y_2O_2S. The lattice parameters refined for Y_2O_2S are consistent with those determined by Zachariasen within the experimental errors.[24] The lattice parameters increase along with an increase in the Eu content of the Eu–Y_2O_2S, since the ionic radius of Eu^{3+} (1.15 Å) is bigger than that of Y^{3+} (1.10 Å).[25] The global reliability factors defined by Young and Wiles[26] are R_{wp} = 16.7% and R_p = 11.8%, and the phase-dependent reliability factors are R_b = 3.8% and R_f = 2.2% for Y_2O_2S, and R_{wp} = 16.0%, R_p = 11.2%, R_b = 4.0% and R_f = 2.3% for the Eu–Y_2O_2S, respectively. Figure 4 shows the manner of fitting between the observed and calculated intensities by the Rietveld analysis for the X-ray powder diffraction pattern of Y_2O_2S, in which the calculated intensities are in fair agreement with the observed values. The manner of fitting for Eu–Y_2O_2S was almost the same as that for Y_2O_2S. Table 4 shows the interatomic distances between Y atoms and oxygen or sulfur atoms of Y_2O_2S. The crystal structures of Y_2O_2S and the Eu–Y_2O_2S are quite similar to that of La_2O_2S.

Table 3. Atomic Parameters of the Crystal Structure of Pure Y_2O_2S

Atom	Site	x	y	z	g	B/Å^2
Y	2d	2/3	1/3	0.2817(8)	1	0.1(1)
O	2d	2/3	1/3	0.630(4)	1	0.3(7)
S	1a	0	0	0	1	0.6(4)

B is the isotropic thermal parameter and g is the site occupancy.

The crystal structure of an unit cell of Y_2O_2S is shown in Fig. 5. In a hexagonal unit cell, two Y atoms sit at sites with C_{3v} symmetry, two O atoms at sites with C_{3v} symmetry,

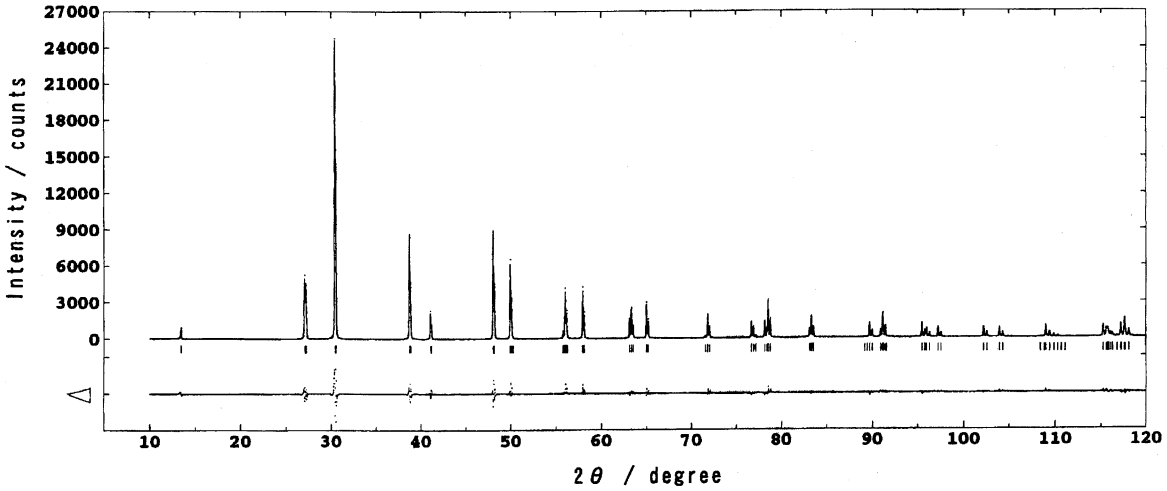

Fig. 4. X-Ray powder diffraction pattern analysed by the Rietveld method. Solid line and dotted line show calculated intensities and observed intensities, respectively. Δ shows the difference between the two.

Table 4. Interatomic Distances between Y Atoms and Oxygen or Sulfur Atoms of Y_2O_2S

Bond	Range (Å)
Y–O	2.29 × 1
Y–O	2.26 × 3
Y–S	2.87 × 3

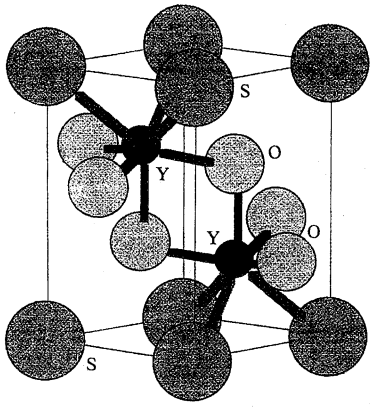

Fig. 5. Schematic crystal structure of Y_2O_2S unit cell.

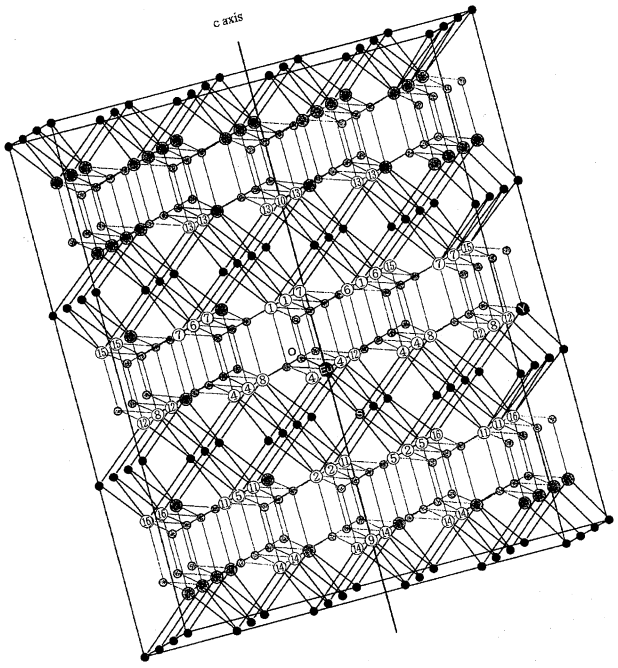

Fig. 6. Eu doped Y_2O_2S. The labeled symbolically 1, 2, 4, 5,⋯, 16 are corresponding to the species with same No. indicated in Table 5.

and one S atom at a site with D_{3d} symmetry. One Y atom is coordinated with four O atoms and three S atoms. For convenience, hereafter, we make a label for each type of Y atom as follows: The central Y atom is named Y^0, the next nearest-neighbor Y atom μ-bridged by O and/or S atoms to Y^0 is Y^1 (i.e., Y^0(–O–, –S–)$\underline{Y^1}$, Y^0–S–$\underline{Y^1}$, etc.), the second nearest-neighbor Y atom μ-bridged by O and/or S atoms to Y^0 is Y^2 (i.e., Y^0(–O–, –S–)Y^1(–O–, –O–)$\underline{Y^2}$, Y^0(–S–, –S–)-Y^1(–S–)$\underline{Y^2}$, etc.) and the third or further far neighboring Y atoms is Y^3, Y^4, ⋯, and so on. If the Eu atom substitutes at one Y site, Eu becomes Eu^0 and the other atoms are named in the same manner. We also labeled each Y atom surrounding one substituted Eu atom as 1, 2, 4, 5, ⋯, 16 in order of the interatomic distance between the Y and Eu, except for No. 5 and No. 6 in Fig. 6. The Y atoms labeled with the same number have the same interatomic distance, but the same number does not always mean that the type of bridge is identical. For example, all Y atoms with number 1 are $\underline{Y^1}$(–O–, –O–)Eu, but Y atoms with number 12 are $\underline{Y^2}$(–O–, –S–)Y^1(–O–, –S–)Eu, or $\underline{Y^2}$(–S–)Y^1(–S–)Eu. The type of the bridge between Y^0 and $\underline{Y}$, the interatomic distance of Y^0–$\underline{Y}$ and the number of $\underline{Y}$ atoms are tabulated in Table 5. The No. of $\underline{Y}$ in Fig. 6 are coressponding to those in Table 5 when Y^0 is replaced by one Eu atom.

Within 6Å of Eu atom there exist four kinds of Y^1, i.e., Eu(–O–, –O–)$\underline{Y^1}$, Eu(–S–, –S–)$\underline{Y^1}$, Eu(–O–, –S–)$\underline{Y^1}$, and Eu–S–$\underline{Y^1}$ and one second nearest-neighbor Y^2, Eu(–O–, –O–)Y^1(–O–, –S–)$\underline{Y^2}$. The four types of Y^1 atoms are attributable to peaks ①, ②, ④, and ⑤, respectively, as discussed later. The Eu–Y distance (r) and the angle (θ) be-

Table 5. The Type of the Bridge between Y^0 and Y, the Interatomic Distance of Y^0–Y, and the Number of Y

No. of Y	Y^0–Y bond	Distance of Y^0–Y/Å	Number of Y
1	Y^0(–O–, –O–)Y^1	3.61	3
2	Y^0(–S–, –S–)Y^1	4.31	3
4	Y^0(–O–, –S–)Y^1	3.78	6
5	Y^0–S–Y^1	5.73	3
6	Y^0(–O–, –S–)Y^1(–O–, –O–)Y^2 Y^0(–O–, –O–)Y^1(–O–, –S–)Y^2	5.23	3
7	Y^0(–O–, –S–)Y^1(–O–, –O–)Y^2 Y^0(–O–, –O–)Y^1(–O–, –S–)Y^2	6.46	6
8	Y^0–S–Y^1(–S–, –S–)Y^2 Y^0(–S–, –S–)Y^1–S–Y^2 Y^0(–O–, –O–)Y^1(–O–, –O–)Y^2 Y^0(–O–, –S–)Y^1(–O–, –S–)Y^2	6.55	6
9	Y^0(–S–, –S–)Y^1(–O–, –O–)Y^2	6.59	1
10	Y^0(–O–, –O–)Y^1(–S–, –S–)Y^2	6.59	1
11	Y^0(–O–, –S–)Y^1(–S–, –S–)Y^2 Y^0(–S–, –S–)Y^1(–O–, –S–)Y^2 Y^0–S–Y^1(–O–, –S–)Y^2	6.87	6
12	Y^0–S–Y^1–S–Y^2 Y^0(–O–, –S–)Y^1(–O–, –S–)Y^2	7.57	6
13	Y^0(–O–, –O–)Y^1(–S–, –S–)Y^2 Y^0(–O–, –O–)Y^1–S–Y^2	7.60	6
14	Y^0(–S–, –S–)Y^1(–O–, –O–)Y^2 Y^0–S–Y^1(–O–, –O–)Y^2	7.60	6
15	Y^0(–O–, –S–)Y^1(–O–, –O–)Y^2(–O–, –S–)Y^3 Y^0–S–Y^1–S–Y^2(–O–, –O–)Y^3	8.39	6
16	Y^0–S–Y^1(–O–, –S–)Y^2 Y^0(–O–, –S–)Y^1–S–Y^2	8.71	6

tween the principal axis at Eu site (crystal *c*-axis) and Eu–Y vector are shown in Table 6, which were used for signal assignments of these 5 species.

Discussion

When Eu atoms were doped in Y_2O_2S, the chemical shift of the central peak ③ in ^{89}Y MAS spectra was kept constant at the position of the pure Y_2O_2S (292 ppm) and the lineshapes were gradually broadened (Fig. 1b). Since the incorporation of paramagnetic Eu^{3+} ions does not cause an isotropic chemical shift to the ^{89}Y signal at 292 ppm, this signal must be free from the Eu effect. We assigned peak ③ to Y^n where Y^n is far apart from Eu (as discussed later, $n \geq 2$). The additional four peaks appear only with Eu doping in Y_2O_2S. Therefore these peaks must result from Y in crystallites containing paramagnetic ions and their chemical shifts are caused by the paramagnetic effect via Eu^{3+} ions with the $4f^6$ electron configuration.

Table 6. The Type of the Bridge between Eu and Y and the Parameters of Structure of Y_2O_2S

Peak No.	Type of the bridge	r[a)] Å	Number of Y atom	Chemical shift/ppm	Δ[b)] ppm	θ[c)] degree	$(3\cos^2\theta-1)/r^3$ 10^{21} cm^{-3}
①	Y^1(–O–, –O–)Eu	3.61	3	367±3	75±2	37.2	19.2
②	Y^1(–S–, –S–)Eu	4.31	3	330±3	38±1	149.5	15.3
③	Y^n ($n \geq 2$)			292±1	0		
④	Y^1(–O–, S–)Eu	3.78	6	231±3	−61±1	90.0	−18.5
⑤	Y^1–S–Eu	5.73	3	142±3	−150±2	130.4	1.40
	Y^2(–O–, –O–)Y^1–(–O–, –S–)Eu	5.23	3	(292)[d)]	(0)	57.0	−7.80

a) r is the Eu–Y interatomic distance calculated by the Rietveld analysis. b) Δ is the difference of chemical shift from the main peak at 292 ppm. − sign represents the lower frequency shift and + sign the higher frequency shift. c) θ is the angle between the principal axis (crystal *c* axis) at the Eu atom and the Eu–Y vector. d) This peak is included in the main peak ③, which is described in the text.

Assignment of the ^{89}Y MAS NMR Signals, $\underline{Y^1}$–Eu Species: As shown in Table 6 and Fig. 6, the population of Eu(–O–, –O–)$\underline{Y^1}$, Eu(–S–, –S–)$\underline{Y^1}$, Eu(–O–, –S–)$\underline{Y^1}$, Eu–S–$\underline{Y^1}$, and Eu(–O–, –O–)Y^1(–O–, –S–)$\underline{Y^2}$ species which exists within 6 Å from Eu atom, is 3, 3, 6, 3, and 3, respectively, per one Eu substituted. According to the relative intensity, 1 : 1 : 2 : 1, of the four peaks ①, ②, ④, and ⑤, peak ④ is assigned to $\underline{Y^1}$(–O–, –S–)Eu. The reduction of T_1 and the shift induced via the paramagnetic Eu^{3+} ion could be useful for further assignments of the three remaining peaks. The spin-lattice relaxation mechanism in a solid containing a paramagnetic species occurs predominantly through the dipolar interaction, rather than through the scalar interaction.[27] The inverse of T_1 is proportional to the inverse of r_j^6:

$$1/T_1 = \sum(2/5)[\gamma_S^2\gamma_I^2\hbar^2S(S+1)][\tau/(1+\omega_I^2\tau^2)]r_j^{-6}, \quad (1)$$

where r_j is the Eu–Y interatomic distance, γ_S and γ_I are the gyromagnetic ratio of the electrons of Eu^{3+} and the Y nucleus, respectively, S is the total electron spin angular momentum of Eu^{3+}, ω_I is the Y nuclear resonance frequency, $\hbar$ is the Plank constant, and τ is T_1 of the unpaired electrons.

T_1 for the four peaks had not any Eu content dependence (Table 2), indicating that the distance between Eu and Y of each species is identical in KR2 to KR6. If we consider Y^1 species including only one Eu, the larger is r, the longer is T_1. In comparison of the observed T_1 (averaged value for 5 samples, see the lowest row in Table 2) to the Eu–Y distance (Table 6), the observed T_1 increases in the order of peak ①<④≤②<⑤, and r increases in the order of Eu(–O–, –O–)$\underline{Y^1}$<Eu(–O–, –S–)$\underline{Y^1}$<Eu(–S–, –S–)$\underline{Y^1}$<Eu(–O–, –S–)Y^1(–O–, –O–)$\underline{Y^2}$<Eu–S–$\underline{Y^1}$. Therefore, peak ① should be assigned to Eu(–O–, –O–)$\underline{Y^1}$, because peak ④ is due to Eu(–O–, –S–)$\underline{Y^1}$. If we assume peak ② is due to Eu(–S–, –S–)$\underline{Y^1}$ and peak ⑤ is due to Eu–S–$\underline{Y^1}$ or Eu(–O–, –O–)Y^1(–O–, –S–)$\underline{Y^2}$ because the latter two species have nearly identical distances (5.73 and 5.23 Å respectively), an inverse of the averaged T_1 for the four peaks can be plotted against $1/r^6$ by using r for each species given in Table 6. Figure 7 demonstrates that $1/T_1$ is well correlated with $1/r^6$, which gives a guarantee for the assumption above. In order to determine which is attributable to peak ⑤, Eu–S–$\underline{Y^1}$ or Eu(–O–, –S–)Y^1(–O–, –O–)$\underline{Y^2}$, the pseudocontact and the contact shifts were discussed as follows.

There are two dominant paramagnetic shifts caused by the incorporation of the Eu atom substituting at the Y atom, the pseudocontact shift[28] via the through-space dipolar interaction and the contact shift[29] via the Fermi interaction. The pseudocontact contribution to the chemical shift of Y^1 or Y^2 resonance via Eu^{3+} ion replacing to Y^0 was estimated as fol-

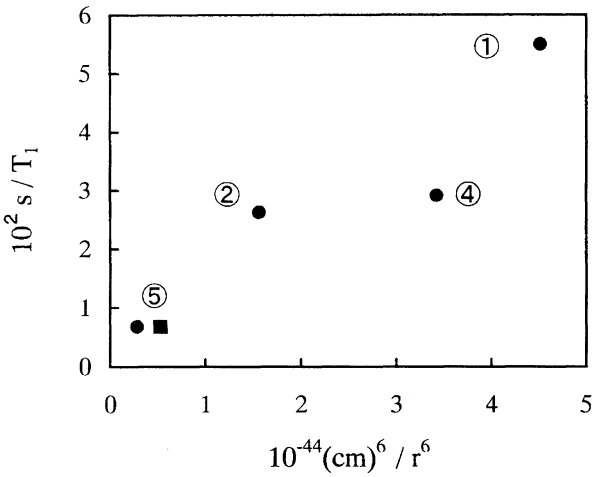

Fig. 7. Relationship between $1/T_1$ and $1/r^6$ for 4 peaks. ● and ■ for peak ⑤ are corresponding to Eu–S–$\underline{Y^1}$ and Eu(–O–, –S–)Y^1(–O–, –O–)$\underline{Y^2}$, respectively.

Table 7. The Relationship between the Bond Style of $\underline{Y^1}$, and the Chemical Shift and T_1

Peak No.	Bond style of $\underline{Y^1}$	Obsd Δ [a] / ppm	Predicted Δ / ppm	Predicted chem. shift / ppm	Obsd chem. shift / ppm	Predicted T_1 / s	Obsd T_1 / s
①	Eu(O,O)$\underline{Y^1}$	75			367		18.2
②	Eu(S,S)$\underline{Y^1}$	38			330		38.2
④	Eu(O,S)$\underline{Y^1}$	−61			231		34.4
⑤	Eu–S–$\underline{Y^1}$	−150			142		148.4
a	Eu(O,O)$\underline{Y^1}$(O,O)Eu		150[b]	442[c]	454	/	/
b	Eu(O,O)$\underline{Y^1}$(S,S)Eu		113	405	406	12[d]	11
c	Eu(S,S)$\underline{Y^1}$(S,S)Eu		76	368	368	/	/
d	Eu(O,O)$\underline{Y^1}$(O,S)Eu		14	306	306	11	/
e	Eu(O,S)$\underline{Y^1}$(S,S)Eu		−23	269	267	20	16
f	Eu(O,O)$\underline{Y^1}$–S–Eu		−75	217	216	14	/
g	Eu(S,S)$\underline{Y^1}$–S–Eu		−112	180	176	34	43
h	Eu(O,S)$\underline{Y^1}$(O,S)Eu		−122	170	168	/	/
i	Eu(O,S)$\underline{Y^1}$–S–Eu		−211	81	75	28	27
j	Eu–S–$\underline{Y^1}$–S–Eu		−300	−8	−11	/	/

a) Δ is the difference of chemical shift from the main peak at 292 ppm. b) The Δ of Eu(O,O)$\underline{Y^1}$(O,O)Eu was estimated as the addition of the Δ of Eu(O,O)$\underline{Y^1}$ and Eu(O,O)$\underline{Y^1}$, i.e., (75+75) = 150 ppm. c) The chemical shift was estimated as (150+292) = 442 ppm. d) T_1 of Eu(O,O)$\underline{Y^1}$(S,S)Eu was estimated as $1/T_1$ (Eu(O,O)$\underline{Y^1}$(S,S)Eu) = $1/T_1$(Eu(O,O)$\underline{Y^1}$)+$1/T_1$(Eu(S,S)$\underline{Y^1}$).

lows: the net pseudocontact shift, ΔH_p, for a paramagnetic ion in axial symmetry is given by[30]

$$\Delta H_p = (-g^2\beta^2 J(J+1)(2J-1)(2J+3)2A_2^0\langle r^2\rangle(3\cos^2\theta - 1) \langle J\|\alpha\|J\rangle H_0)/(60(kT)^2 r^3), \quad (2)$$

where g is the Lande g factor, J quantum number of a total angular momentum of the paramagnetic ion, $A_2^0\langle r^2\rangle$ a crystal field parameter, r the Eu–Y distance, θ the angle between the principal axis at Eu and the Eu–Y vector, and $\langle J\|\alpha\|J\rangle$ a numerical coefficient. It is predicted that the psuedocontact shift due to Eu^{3+} is zero as $J = 0$ at ground state. Because Eu^{3+} is known to have low-lying excited J states, a more refined interaction term involving excited states for Eu^{3+} has included.[29] In (Y, Ln)$_2$Ti$_2$O$_7$ and (Y, Ln)$_2$Sn$_2$O$_7$ (Ln: Eu, Nd) three peaks were observed, which are caused by $\underline{Y}(OY)_5(OLn)$ species, and their shifts were explained mainly by the pseudocontact interaction.[4] We thus tried to explain the shift of the four peaks by the pseudocontact mechanism first. In Eq. 2, the contribution from the structural term, $(3\cos^2\theta - 1)/r^3$, is calculated from the crystal structure data, which was listed in Table 6. Assuming that the other parameters in Eq. 2 are constant for all species, the pseudocontact shift becomes proportional to the value of the structural term, $(3\cos^2\theta - 1)/r^3$. The pseudocontact shift estimated is in order of $\underline{Y^1}$(–O–, –O–)Eu (peak ①)>$\underline{Y^1}$(–S–, –S–)Eu (peak ②)>$\underline{Y^1}$–S–Eu>$\underline{Y^2}$(–O–, –S–)Y^1(–O–, –O–)Eu>$\underline{Y^1}$(–O–, –S–)-Eu (peak ④) from higher frequency side. As mentioned above, peaks ①, ② and ④ have already been assigned on the basis of T_1 and the relative signal intensity. The estimated pseudocontact shifts for peaks ①, ②, and ④ are in the order of the observed shifts. Peak ⑤ exhibited an extremely lower frequency shift in comparison with the pseudocontact shift estimated for $\underline{Y^1}$–S–Eu or $\underline{Y^2}$(–O–, –O–)Y^1(–O–, –S–)Eu. This fact suggests the presence of any other reason, such as some difference of the crystal field parameter, $A_2^0\langle r^2\rangle$, and difference in the degree of the contribution due to the contact shift in $\underline{Y^1}$–S–Eu or $\underline{Y^2}$(–O–, –O–)Y^1(–O–, –S–)Eu from those in other three species.

According to the estimated pseudocontact shift, a peak originated by $\underline{Y^2}$(–O–, –O–)Y^1(–O–, –S–)Eu should be detected between peak ③ and peak ④. However any other peak with enough intensity was not observed. In the discussion above, we assumed the identical $A_2^0\langle r^2\rangle$ for both types of species despite the difference in interatomic distance r between $\underline{Y^2}$(–O–, –O–)Y^1(–O–, –S–)Eu and other four Y^1 species such as $\underline{Y^1}$(–O–, –O–)Eu. Therefore, the pseudocontact shift for the Y^2 species must be overestimated, because the crystal field parameter becomes smaller for $\underline{Y^2}$(–O–, –O–)Y^1(–O–, –S–)Eu with longer distance (5.23 Å) than for $\underline{Y^1}$(–O–, –O–)Eu (3.61 Å). The chemical shift of the signal for $\underline{Y^2}$(–O–, –O–)Y^1(–O–, –S–)Eu must move toward to the main peak ③ and actually could overlap to peak ③. As for the other $\underline{Y^2}$–Eu species, which are shown in Fig. 6, the estimated pseudocontact shifts from the structural parameter under the same assumption are distributed in the range from -7.85 to 6.99×10^{21} cm^{-3}, compared with -18.5 to 19.2×10^{21} cm^{-3} for $\underline{Y^1}$–Eu species. In the same manner the reduction of $A_2^0\langle r^2\rangle$ value for $\underline{Y^2}$–Eu species causes to move their shift towards to peak ③. Namely, we conclude that all Y^n ($n\geq2$) signals are included in peak ③.

The contact shift due to the Fermi interaction with the unpaired electrons is written as follows:[29]

$$\Delta H_c = a_n\langle S_z\rangle/(\gamma\hbar), \quad (3)$$

where a_n is the electron-nuclear hyperfine coupling constant, $\langle S_z\rangle$ the expectation value of the z component of the Eu^{3+} spin, γ the gyromagnetic ratio, and $\hbar$ the Planck constant. In Eq. 3 only a_n is strongly dependent on the nature of the bond between Eu^{3+} and the given nuclei, in other words, on a degree of delocalization of unpaired electrons through each bond connecting Eu and Y atoms. Therefore, the contact shift will quickly fall down as the number of bonds separating the resonating Y from the paramagnetic ion increases. $\underline{Y^1}$–S–Eu has two bonds connected straightly through the S atom between $\underline{Y^1}$ and the Eu atoms, while $\underline{Y^2}$(–O–, –S–)-Y^1(–O–, –O–)Eu has two sets of four zigzag bonds between them. The big lower frequency shift observed in peak ⑤ is attributable to the contact shift in to $\underline{Y^1}$–S–Eu, not to $\underline{Y^2}$(–O–, –O–)Y^1(–O–, –S–)Eu. We assigned peak ⑤ to $\underline{Y^1}$–S–Eu.

Assignment of the ^{89}Y MAS NMR Signals, Eu–$\underline{Y^1}$–Eu Species: We discussed above the Y^1 species with only one Eu atom in the next nearest-neighbor Y. In samples with the higher Eu content, however, Y^1 species with two next nearest-neighbor Eu atoms are possibly produced. According to the crystal structural data, there exist ten such species with different bonding property, i.e., Eu(–O–, –O–)Y^1(–O–, –O–)Eu, Eu(–O–, –O–)Y^1(–S–, –S–)Eu, Eu-(–S–, –S–)Y^1(–S–, –S–)Eu, Eu(–O–, –O–)Y^1(–O–, –S–)-Eu, Eu(–O–, –S–)Y^1(–S–, –S–)Eu, Eu–S–Y^1(–O–, –O–)Eu, Eu–S–Y^1(–S–, –S–)Eu, Eu(–O–, –S–)Y^1(–O–, –S–)Eu, Eu-(–O–, –S–)Y^1–S–Eu and Eu–S–Y^1–S–Eu. Chemical shifts of ten species can be estimated by an additivity of the paramagnetic shifts for each bond property included in an individual species, i.e., the observed shift of four Y^1 species mentioned above. The predicted chemical shift is listed up in Table 7. As demonstrated in Fig. 3, we detected ten peaks with short T_1 by employing the short recycle time. Surprisingly, the observed chemical shift of ten peaks labeled by (a), (b), (c), - - - and (j) is perfectly fitted to the predicted chemical shift. Therefore, the peaks (a) to (j) were assigned to Eu–Y^1–Eu species. The good agreement in the predicted and the observed chemical shifts of ten species enforces the certainty of the assignment of peak ⑤ to $\underline{Y^1}$–S–Eu.

Distribution of Eu Atoms: One Eu atom doped in pure Y_2O_2S creates fifteen Y^1 atoms around the Eu through O and/or S bridges. If we assume a random distribution of Eu in Y_2O_2S, the ratio of the number of Y^1 atoms to Y^n ($n\geq2$) atoms is calculated as $Y^1 : Y^n = 15c : (1-16c)$ for $(Y_{1-c}, Eu_c)_2O_2S$. Under this assumption there exist only the Y^1–Eu and Y^n ($n\geq2$) species when $c<0.625$, i.e., sample KR1 to KR4 and Y^1–Eu and Eu–Y^1–Eu species exist only when

$c>0.625$ i.e., KR5, KR6, and moreover, and no Y^n ($n\geq 2$) species exist in samples KR5 and KR6. In the experimental observation, nevertheless, peak ③ still had a significant intensity in all samples. Moreover, if we compare the calculated Y^1/Y^n with the observed Y^1/Y^n in ^{89}Y NMR, which are presented in Table 2, the observed Y^1/Y^n is smaller than the calculated one even in the sample with very low Eu content. These results suggest that the doped Eu atoms are not always distributed randomly and a portion of the Eu atoms could not affect to ^{89}Y resonance. Here, in Eu–Y_2O_2S, the model which we proposed in Tb–$Y_3Al_5O_{12}$ green phosphor and Eu–Y_2O_3 red phosphor could be justified.[16,17] Namely the doped Eu atoms form a randomly distributed area, where Eu atoms are sufficiently separated from each other, and a densely distributed area, where Y atoms are surrounded by more than three of next nearest-neighbor Eu atoms and do not contribute to ^{89}Y NMR spectra. Both areas are always present as a mixture. If we assume that the randomly distributed area forms its own block in the sample and the observed Y^1/Y^n ratio originates in the area, an actual component of Y and Eu in the randomly distributed area would be calculated as ($Y_{0.987}$, $Eu_{0.013}$) in KR3, ($Y_{0.977}$, $Eu_{0.023}$) in KR4, ($Y_{0.969}$, $Eu_{0.031}$) in KR5, and ($Y_{0.964}$, $Eu_{0.036}$) in KR6, which is tabulated in Table 2. We can not say about how many percentage of the Eu atoms doped in each sample belong to the area from the present data. A quantitative analysis of the signal intensity would be necessary.

T_1 and the Line-Broadening of Peak ③: The spin-lattice relaxation rate, $1/T_1$, as described by Eq. 1, is approximately proportional to r_j^{-6}, that is, square of Eu content, $[Eu]^2$. The plot of $1/T_1$ (closed circle) versus [Eu content]^2 in Fig. 8 showed a curvature especially in the small amount Eu content. If we take the Eu content estimated from the Y^1/Y^n ratio as an effective Eu concentration (Eu_{eff}), the plot of $1/T_1$ (open square) versus [Eu_{eff} concentration]^2 showed a much better linear relation in all content range, as shown in Fig. 8. Namely, only the paramagnetic centers incorporated randomly in the mother crystallites affect to the T_1 reduction of peak ③.

The line-broadening arising from the magnetic moment of the electron is caused primarily by the interaction between the magnetic dipoles, which was described based on the second moment method by Van Vleck.[31] The second moment, M_2, for the interaction between the electron spin of Eu^{3+} and the Y nuclear spin is related to the interatomic distance r_j (Eu–Y) as follows:

$$M_2 = (4/15)\gamma_S^2\gamma_I^2\hbar^2 S(S+1)\sum r_j^{-6}. \quad (4)$$

Since the dipolar line-broadening is proportional to a square root of M_2, and then approximately proportional to r_j^{-3}, even in the lattice where the paramagnetic centers were not distributed in the cubic symmetry, the dipolar line-broadening becomes proportional to the content of Eu^{3+} ions, $[Eu^{3+}]$. The linewidth at the half-height of the central peak ③ plotted versus the Eu content showed a good linear relation, as shown in Fig. 2. If we plot the linewidth versus Eu_{eff} concentration estimated above, a lower convexed curve is obtained and no linear relation is exist. This indicates that the randomly distributed area and the densely distributed area are well mixed in microscopic scale and the line-broadening is affected by whole Eu atoms or that a constant percentage of the doped Eu content in each sample is distributed in the randomly oriented area. In contrast to the T_1 reduction, where closely present Eu atoms became affective, the line-broadening was caused by Eu ions far from Y atoms.

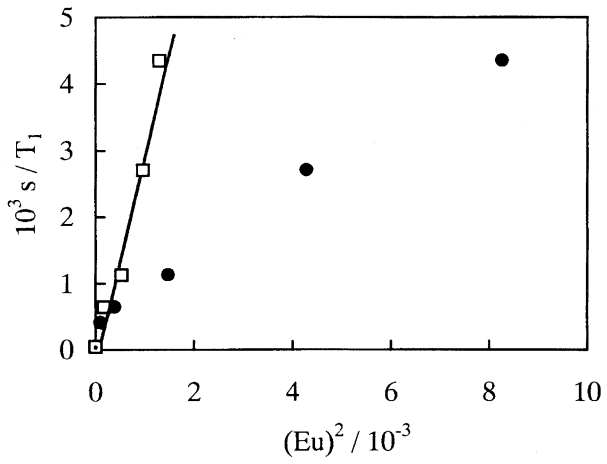

Fig. 8. Relationships between $1/T_1$ for peak ③, and [Eu content]^2 and [Eu_{eff} concentration]^2. ● and □ indicate the incorporated Eu content and the estimated effective Eu concentration, respectively.

Brightness of Eu–Y_2O_2S: In the phosphors, generally, the concentration-quenching effect decreases the emission intensity when the Eu–Eu distance becomes shorter.[18] In the present investigation, the emission intensity at 624 nm by excitation via UV (254 nm) increased with the Eu content and then decreased in the samples with high Eu content. As mentioned above, NMR becomes inactive for Y atoms in the densely Eu distributed area where the concentration-quenching effect occurs.

Conclusions

Solid state ^{89}Y ($I = 1/2$) MAS NMR of the red phosphor, Eu–Y_2O_2S, have been investigated for the characterization of Y sites in the phosphor. Besides the main peak (292 ppm) by Y^n ($n\geq 2$) species in pure Y_2O_2S, another 4 peaks appeared in the Eu–Y_2O_2S up to 10 mol%. Upon increasing the Eu content, 10 smaller peaks appeared. Before assignment of these peaks the crystal structure of the samples was precisely investigated by the Rietveld method. The crystal structures of Y_2O_2S and the Eu–Y_2O_2S are quite similar to that of La_2O_2S and the all observed ^{89}Y MAS NMR peaks have been assigned to Y atoms specifically positioned to the doped Eu atoms. The previous 4 peaks are attributable to $\underline{Y^1}$–Eu species, i.e., $\underline{Y^1}$(–O–, –O–)Eu (367 ppm), $\underline{Y^1}$(–S–, –S–)Eu (330 ppm), $\underline{Y^1}$(–O–, –S–)Eu (231 ppm), and $\underline{Y^1}$–S–Eu (142 ppm). The relative intensity and chemical shifts of the 4 peaks, and relationships between T_1 and structural parameters (Y–Eu distance, the angle be-

tween the Eu–Y^1 vector and the principal axis at the Eu site, and the bond angle of Eu–O–Y and/or Eu–S–Y) are mutually used for the assignment. The 10 peaks appearing in the spectra measured at rather short recycle times for samples with higher Eu content are assigned to Y^1 with two Eu atoms in the fifteen next nearest-neighbor Y sites, that is, from higher frequency side Eu(–O–, –O–)$\underline{Y^1}$(–O–, –O–)Eu (454 ppm), Eu(–O–, –O–)$\underline{Y^1}$(–S–, –S–)Eu (406 ppm), Eu(–S–, –S–)$\underline{Y^1}$(–S–, –S–)Eu (368 ppm), Eu(–O–, –O–)$\underline{Y^1}$(–O–, –S–)Eu (306 ppm), Eu(–O–, –S–)$\underline{Y^1}$(–S–, –S–)Eu (267 ppm), Eu–S–$\underline{Y^1}$(–O–, –O–)Eu (216 ppm), Eu–S–$\underline{Y^1}$(–S–, –S–)Eu (176 ppm), Eu(–O–, –S–)$\underline{Y^1}$(–O–, –S–)Eu (168 ppm), Eu(–O–, –S–)$\underline{Y^1}$–S–Eu (75 ppm) and Eu–S–$\underline{Y^1}$–S–Eu (−11 ppm). The signals for Y^1 with more than three next nearest-neighbor Eu to Y^1 was not found at the predicted position. The signals for $\underline{Y^2}$ species such as $\underline{Y^2}$(–O–, –O–)Y^1(–O–, –S–)Eu, where Y^2 is the second nearest-neighbor Y to Eu, were not separately detected from the central peak, because their predicted peak positions are very close to the central peak. It is clear that paramagnetic Eu^{3+} ions do not affect to the chemical shift of the signal for Y^n ($n \geq 2$) in Eu–Y_2O_2S. The chemical shift of these peaks was discussed based on the pseudocontact and the contact shift mechanisms. Especially the species Eu–S–$\underline{Y^1}$ exhibits rather large contact shift than other species because of its straight bonding between Eu and Y. The paramagnetic Eu^{3+} incorporation results a huge reduction of T_1 values of ^{89}Y signal from 6.6 h for pure Y_2O_2S to 230 s (10 mol% Eu–Y_2O_2S) for main peak (Y^n: $n \geq 2$ species), to several tens of seconds for $\underline{Y^1}$–Eu, and to several seconds for Eu–$\underline{Y^1}$–Eu in Eu–Y_2O_2S at high Eu content. The T_1 reduction is mainly attributable to the dipolar interaction between the paramagnetic Eu^{3+} ion and ^{89}Y nuclei and not to a spin diffusion mechanism.

An investigation for NMR-active Y atoms are mostly necessary for design of high emission intensity. Quantitative investigation of signal intensities of newly appeared signals, the reduction of T_1 and the line-broadening due to incorporated paramagnetic Eu^{3+} ions in ^{89}Y NMR spectra will be promising technique for solving the problem, how we can obtain the high brightness of phosphor Eu–Y_2O_2S.

We wish to thank Mr. Yasuo Shimomura (Mitsubishi Chemical Co., Ltd.) for the measurement of UV-excited luminescence for Eu–Y_2O_2S.

References

1 V. P. Chacko, S. Ganapathy, and R. G. Bryant, *J. Am. Chem. Soc.*, **105**, 5491 (1983).

2 S. Yang, J. Shore, and E. Oldfield, *J. Magn. Reson.*, **99**, 408 (1992).

3 C. P. Grey, C. M. Dobson, A. K. Cheetham, and R. J. B. Jakeman, *J. Am. Chem. Soc.*, **111**, 505 (1989).

4 C. P. Grey, M. E. Smith, A. K. Cheetham, C. M. Dobson, and R. Dupree, *J. Am. Chem. Soc.*, **112**, 4670 (1990).

5 Z. P. Han, R. Dupree, D. M. Paul, A. P. Howes, and L. W. J. Caves, *Physica C*, **181**, 355 (1991).

6 K. Liu, D. Ryan, K. Nakanishi, and A. McDermott, *J. Am. Chem. Soc.*, **117**, 6897 (1995).

7 Y. J. Lee, F. Wang, and C. P. Grey, *J. Am. Chem. Soc.*, **120**, 12601 (1998).

8 A. Nayeem and J. P. Yesinowski, *J. Chem. Phys.*, **89**, 4600 (1988).

9 G. V. M. Williams and J. L. Tallon, *Phys. Rev.*, **B57**, 8696 (1998).

10 G. Balakrishnan, L. W. J. Caves, R. Dupree, D. M. Paul, and M. E. Smith, *Physica C*, **161**, 9 (1989).

11 A. R. Thompson and E. Oldfield, *J. Chem. Soc., Chem. Commun.*, **1987**, 27.

12 R. Dupree and M. E. Smith, *Chem. Phys. Lett.*, **148**, 41 (1988).

13 P. D. Battle, B. Montez, and E. Oldfield, *J. Chem. Soc., Chem. Commun.*, **1988**, 584.

14 K. J. D. MacKenzie and R. H. Meinhold, *J. Mater. Chem.*, **4**, 1595 (1994).

15 T. Harazono and T. Watanabe, *Bull. Chem. Soc. Jpn.*, **70**, 2383 (1997).

16 T. Harazono, E. Yokota, H. Uchida, and T. Watanabe, *Bull. Chem. Soc. Jpn.*, **71**, 825 (1998).

17 T. Harazono, E. Yokota, H. Uchida, and T. Watanabe, *Bull. Chem. Soc. Jpn.*, **71**, 2797 (1998).

18 "Handbook of Phosphors," ed by Phosphor Research Society, Ohm Co., Ltd., Tokyo (1987), p. 259 (preparation), p. 78 (concentration quenching).

19 T. Harazono, E. Yokota, Y. Tokunaga, R. Adachi, and A. Hase, "Yttrium Oxysulfide Phosphor," Japan Patent 325569, 1996.

20 T. Harazono, T. Mori, and R. Adachi, "Yttrium Oxysulfide Phosphor," Japan Patent 110166, 1998.

21 F. Izumi, *J. Crystallogr. Soc. Jpn.*, **27**, 23 (1985).

22 S. Imanaga, S. Yokono, and T. Hoshina, *J. Lumin.*, **16**, 77 (1978).

23 T. Hoshina, "Luminescence of Lanthanoid Ions," ed by Sony Research Center Reports, Supplement, Yokohama (1983), p. 61.

24 W. H. Zachariasen, *Acta Crystallogr.*, **2**, 60 (1949).

25 J. E. Huheey, "Inorganic Chemistry, Principles of Structure and Reactivity," Harper & Row, Publishers, New York (1978), p. 71.

26 R. A. Young and D. B. Wiles, *J. Appl. Crystallogr.*, **15**, 430 (1982).

27 A. Abragam, "Principles of Nuclear Magnetism," the Clarendon Press, Oxford (1961), Chap. 9.

28 B. J. Bleaney, *J. Magn. Reson.*, **8**, 91 (1972).

29 R. M. Golding and M. P. Halton, *Aust. J. Chem.*, **25**, 2577 (1972).

30 B. Bleaney, C. M. Dobson, B. A. Levine, R. J. P. Williams, and A. V. Xavier, *J. Chem. Soc., Chem. Commun.*, **1972**, 791.

31 J. H. Van Vleck, *Phys. Rev.*, **74**, 168 (1948).

32 Specification of Colors according to the Commision Internationale de l'Eclairage (CIE) 1931. JIS handbook 33, "Colors" Z8701-1982, ed by Japan Society of Standard, p. 117.